Tunable multiferroic order parameters in $Sr_{1-x}Ba_xMn_{1-y}Ti_yO_3$

Kamal Chapagain,[1,*] Dennis E. Brown,[1] Stanislaw Kolesnik,[1] Saul Lapidus,[2] Bianca Haberl,[3] Jamie Molaison,[3] Chuanlong Lin,[4,†] Curtis Kenney-Benson,[5] Changyong Park,[5] Jaroslaw Pietosa,[6] Ewa Markiewicz,[7] Bartlomiej Andrzejewski,[7] Jeffrey W. Lynn,[8] Stephan Rosenkranz,[9] Bogdan Dabrowski,[6] and Omar Chmaissem[1,9]

[1]*Department of Physics, Northern Illinois University, DeKalb, Illinois 60115, USA*

[2]*X-ray Science Division, Advanced Photon Source, Argonne National Laboratory, Lemont, Illinois 60439, USA*

[3]*Neutron Scattering Division, Neutron Sciences Directorate, Oak Ridge National Laboratory, Oak Ridge, Tennessee 37830, USA*

[4]*Geophysical Laboratory, Carnegie Institution of Washington, Washington, DC 20015, USA*

[5]*HPCAT, X-ray Science Division, Advanced Photon Source, Argonne National Laboratory, Lemont, Illinois 60439, USA*

[6]*Institute of Physics, Polish Academy of Sciences, Aleja Lotnikow 32/46, PL-02668 Warsaw, Poland*

[7]*Institute of Molecular Physics, Polish Academy of Sciences, Smoluchowskiego 17, PL-60179 Poznań, Poland*

[8]*NIST Center for Neutron Research, National Institute of Standards and Technology, Gaithersburg, Maryland 20899-6102, USA*

[9]*Materials Science Division, Argonne National Laboratory, Lemont, Illinois 60439, USA*

(Received 22 May 2019; published 1 August 2019)

Responding to the rapidly increasing demand for efficient energy usage and increased speed and functionality of electronic and spintronic devices, multiferroic oxides have recently emerged as key materials capable of tackling this multifaceted challenge. In this paper, we describe the development of single-site manganese-based multiferroic perovskite materials with modest amounts of nonmagnetic Ti substituted at the magnetic Mn site in $Sr_{1-x}Ba_xMn_{1-y}Ti_yO_3$ (SBMTO). Significantly enhanced properties were achieved with ferroelectric-type structural transition temperatures boosted to ∼430 K. Ferroelectric distortions with large spontaneous polarization values of $\sim 30\,\mu C/cm^2$, derived from a point charge model, are similar in magnitude to those of the prototypical nonmagnetic $BaTiO_3$. Temperature dependence of the system's properties was investigated by synchrotron x-ray powder diffraction and neutron powder diffraction at ambient and high pressures. Various relationships were determined between the structural and magnetic properties, Ba and Ti contents, and T_N and T_C. Most importantly, our results demonstrate the large coupling between the magnetic and ferroelectric order parameters and the wide tunability of this coupling by slight variations of the material's stoichiometry.

DOI: 10.1103/PhysRevMaterials.3.084401

I. INTRODUCTION

Highly flexible perovskite-based platforms (ABO_3 with A = alkaline or rare earth metal, B = transition metal) have repeatedly proven their worth by accommodating an impressive number of chemical elements in a very simple and elegant structure with distortions that can be engineered to produce an incredible wealth of functional properties, including superconductivity, ferroelectricity (FE), ferromagnetism, and ferroelasticity [1–4], just to name a few. Single ferroic materials are naturally abundant, but the coexistence of two or more ferroic orders, especially with both the desired FE and magnetic properties [4–8], is quite scarce. One reason for the severe shortage of multiferroic compositions was due to the conflicting dual need for both d^0 and d^n transition metal elements, essential for conventional ferroelectricity and magnetism, respectively [9]. Thus, the recent development of multiferroic $BiMnO_3$, $BiFeO_3$, $YMnO_3$, and $TbMnO_3$ perovskites [5,7,10–14] in which both order parameters are realized has been received with great interest because of the unique opportunity they present in bringing us closer to understanding the driving mechanisms responsible for their coexistence, in addition to their potential for practical applications where magnetic properties are controlled electrically and vice versa [6,15–17].

$BiFeO_3$ is one of perhaps the most popular multiferroic systems because of its very high FE transition temperature (∼1100 K), due to Bi $6s^2$ lone pairs, and an exotic cycloidal antiferromagnetic structure (AFM) arising from exchange interactions between the localized magnetic moments of Fe $d^5 = t^3e^2$ electrons. The ordering of ferroelectricity and magnetism on two separate sublattices renders the magnetoelectric coupling quite weak [18]. Recent $BiFeO_3$ thin films were successfully grown to exhibit stronger multiferroic correlations [7,19]. However, and despite their promising potential, the functionality of $BiFeO_3$ thin films remains severely limited by the persistence of detrimental leakage currents caused by the additional charge carriers produced by the volatile Bi^{3+} cationic off-stoichiometry [20,21]. Moreover, $BiFeO_3$ thin films tend to form robust magnetic domains which result in the undesirable multistep reversal of the FE moment when subjected to external electric fields [20,21]. While recent work demonstrates that the latter problem may be overcome by growing $BiFeO_3$ films on ⟨111⟩-oriented $TbScO_3$ substrates [22], it is clear that the development of alternate systems with strongly coupled multiferroic properties remains a priority.

*Corresponding author: chapkamal@gmail.com

†Present address: Center for High Pressure Science and Technology Advanced Research, Beijing 100094, China.

Recent first-principle calculations suggested the possible realization of FE distortions in the inherently magnetic $AMnO_3$ manganites ($A = Ba^{2+}$, Sr^{2+}, or Ca^{2+}) [23–27]. Unusually large electric polarization properties were predicted, approaching those of the prototypal displacive-type $BaTiO_3$ ferroelectrics. For example, ferroelectricity with a spontaneous polarization of $12.8\,\mu C/cm^2$ was speculated by forcing the off-centering of the Mn^{4+} ions in the hypothetical $BaMnO_3$ perovskite structure [25]. Unfortunately, and to the best of our knowledge, only nonferroelectric hexagonal $BaMnO_3$ polymorphs (2L, 4L, 6L etc.) have to date been synthesized, while the anticipated pseudocubic analogs remain elusive (see Ref. [28], for example). In the case of antiferromagnetic $SrMnO_3$ and $CaMnO_3$, several groups suggested the theoretical stabilization of ferroelectricity in epitaxially strained thin films [23,24,29].

Strain-induced ferroelectricity could also be produced through the chemical engineering of desired pressures in substituted bulk materials. Studies performed over an extensive range of substitutions have shown strong correlations between the ionic size and the resulting magnetic and structural properties of the perovskite materials [30–32]. With substitution of larger Ba (1.61 Å) for Sr (1.44 Å) [33], we successfully induced FE in bulk AFM $Sr_{1-x}Ba_xMnO_3$ perovskites ($x > 0.4$) in which the Mn-O bonds are subjected to considerably larger tensile strains than those typically observed by Ti-O bonds in the $BaTiO_3$ ferroelectric analog. Our results are in remarkable agreement with Sakai *et al.*'s [34] reported ferroelectricity in $Sr_{1-x}Ba_xMnO_3$ single crystals with $x = 0.45$ and 0.50 grown using the floating zone image furnace technique. $Sr_{1-x}Ba_xMnO_3$ samples with $x \leqslant 0.4$ are not ferroelectric despite the significant strains surrounding the MnO_6 octahedra [31,35].

The transition temperature from paraelectric to ferroelectric $Sr_{1-x}Ba_xMnO_3$ changes steeply, from 345 to 410 K, as a function of small variations of the Ba content within a narrow composition range $0.43 \leqslant x \leqslant 0.5$ [34,35]. Ferroelectric ordering coincides with a structural transition from centrosymmetric cubic $Pm\bar{3}m$ to the lower symmetry of noncentrosymmetric tetragonal $P4mm$ ($T_{\text{Cubic}\rightarrow\text{Tetragonal}} \equiv T_S$), similar to that of the prototypical nonmagnetic $BaTiO_3$. Although strongly suppressed below the AFM Néel transition temperature ($T_N \sim 200$ K), the FE order remains present as confirmed by neutron and x-ray powder diffraction [35,36] and *P-E* hysteresis curves measured only at 2 K due to considerable leakage currents [34]. The spontaneous polarization P_S of $\sim 13.5\,\mu C/cm^2$ measured along the c axis for $x = 0.5$ [34] was roughly half the maximum polarization $\sim 25\,\mu C/cm^2$ estimated from the empirical relation $P_S^2 \propto (c/a - 1)$ [34] in the FE-only temperature range above T_N. Similar values were calculated using neutron-diffraction results [35,36]. The ability of the magnetic order to drastically reduce ferroelectricity demonstrates a strong and robust magnetoelectric coupling, as discussed in recent *ab initio* calculations [26,27]. Infrared (IR) optical measurements and inelastic x-ray scattering of polycrystalline $Sr_{1-x}Ba_xMnO_3$ samples confirm the existence of strong spin-phonon and magnetoelectric coupling below T_N [37–39]. The FE polarization and magnetoelectric coupling increases with Ba substitution [35].

Unfortunately, because of the severely unfavorable size contrast between Ba^{2+} and Sr^{2+}, it has proven difficult to extend the Ba solubility limit at ambient pressure to $x > 0.45$ [40]. To overcome these synthesis limitations, reduce leakage currents, and weaken magnetism, which suppresses ferroelectricity, dilute amounts of nonmagnetic Ti were added at the Mn site, allowing us to successfully develop a $Sr_{1-x}Ba_xMn_{1-y}Ti_yO_3$ (SBMTO) series with tunable magnetoelectric coupling strength and properties. In this paper, we report the multiferroic properties of SBMTO with x extended to 0.7 and y restricted to remain in the dilute limit between 0 and 0.12. Robust FE properties are obtained with T_S increasing to $\sim$430 K together with larger tetragonal distortions suggesting P_S values greater than those of the Ti-free $Sr_{1-x}Ba_xMnO_3$ counterparts. The onset of magnetic ordering, on the other hand, decreases slightly to $\sim$142 K due to local disruptions of the magnetic Mn sublattice by nonmagnetic Ti^{4+} substituents. Titanium substitution is demonstrated to be an effective tuning knob for the magnetoelastic coupling strength below T_N. A combination of pressure-dependent magnetic measurements and neutron and x-ray diffraction demonstrate the strong coupling between the two order parameters.

II. EXPERIMENTAL DETAILS

Single-phase polycrystalline $Sr_{1-x}Ba_xMn_{1-y}Ti_yO_3$ samples with $x = 0.43-0.70$ and $y = 0.0-0.12$ were synthesized from stoichiometric mixtures of $BaCO_3$ (99.9% pure), $SrCO_3$ (99.99%), MnO_2 (99.95%), and TiO_2 (99.99%). Mixtures were homogenized by agate ball milling in ethanol for 6 hours. The dried powder was then ground and calcined at 1000−1200 °C for 10 hours. After calcination, the powder was reground and pressed into pellets of $\sim$2−3 mm thickness and $\sim$11 mm diameter and sintered for 12 hours at 1200−1450 °C. A two-step synthesis method, described in Refs. [31,41], was used to overcome the hexagonal phase and stabilize the FE distorted perovskite structure. First, single-phase oxygen-deficient perovskites were produced after several grinding and heating cycles in reducing Ar/H_2 atmospheres at 1250−1450 °C. Next, the oxygen-deficient samples were annealed in air or oxygen at 350−450 °C followed by slow cooling to ensure a total of 3.00 ± 0.01 oxygen atoms per formula unit. The oxygen full stoichiometry of our samples was determined by careful measurements of the mass before and after annealing. Sample purity and phase formation were determined at room temperature by x-ray diffraction using a Rigaku powder diffractometer (XRD) with Cu $K\alpha$ wavelength radiation.

Temperature-dependent structural properties of a few select samples were investigated using the high-resolution 11-BM-B powder diffractometer at the Advanced Photon Source of Argonne National Laboratory. Data sets were collected in a wide temperature range 80–452 K using an x-ray beam of wavelength 0.4142 Å ($\sim$30 keV). Hysteresis of the structure affecting T_S and FE was carefully examined for the $x = 0.55$, $y = 0.05$ sample via a heating/cooling cycle with ramp rates of $\pm 0.6°$/ min. The same sample was also measured under pressure and low temperature at the 16-BM-D beamline [42] of the High Pressure Collaborative Access Team (HPCAT) at the Advanced Photon Source using an x-ray beam of wavelength 0.4246 Å (29.2 keV). Data were reduced to one-dimensional (1D) profiles using DIOPTAS [43]. A symmetric

diamond-anvil cell (DAC) was used to generate pressures in the range of 0.8–2.02 GPa at temperatures between 120 and 298 K. The DAC was loaded at the APS's GeoSoilEnviroCARS gas loading facilities using neon serving as the hydrostatic pressure-transmitting medium [44]. Pressure was determined using the ruby fluorescence method and typical temperature corrections [45,46]. Cooling was achieved in an HPCAT cryostat, and pressure increase/control was performed through a dual-membrane system [47].

Further pressure measurements were carried out on the Spallation Neutrons and Pressure diffractometer (SNAP) at the Spallation Neutron Source of Oak Ridge National Laboratory [48]. A 0.25-g sample of the same $Sr_{0.45}Ba_{0.55}Mn_{0.95}Ti_{0.05}O_3$ material was loaded in a Paris-Edinburgh (PE) pressure cell equipped with single-toroidal anvils made from cubic boron nitride. An encapsulated gasket made from null-scattering TiZr was used. The sample was loaded together with a 4:1 mixture of deuterated methanol:ethanol liquid medium and measured at hydrostatic pressures and temperatures ranging between ~0.5 and 6 GPa and 90 and 250 K, respectively. The pressure was determined from a very carefully calibrated pressure-load curve measured on the same sample material using the same gasket/anvil setup and same pressure medium. The pressure was extracted using the equation of state obtained from the x-ray diffraction data. Care was taken to determine the onset of plastic deformation of the gasket, i.e., the load at which pressure on the sample increased measurably, in order to obtain reliable low-pressure measurements. Cooling was performed through SNAP's copper cooling clamps that essentially flow liquid nitrogen around the PE anvils. The time-of-flight data were reduced and normalized using typical SNAP procedures in MANTID [49]. Rietveld refinements were performed using the software suite GSAS/EXPGUI [50,51]. Direct current (DC) and alternating current (AC) magnetic measurements were carried out in fields up to 7.0 T using Magnetic Property Measurement Systems (MPMS) by Quantum Design. Hydrostatic pressure was applied using an easyLab MCell10 pressure cell with Daphne 7373 oil. A high-purity Sn wire (0.25 mm in diameter) was employed as an *in situ* manometer.

Magnetic order parameter scans were collected on the BT-7 spectrometer at ambient pressure at the National Institute of Standards and Technology (NIST) Center for Neutron Research (NCNR) using an energy of 14.7 meV, coarse collimation, and a position-sensitive detector [52]. Additional data were collected on the high-resolution powder diffractometer BT-1 for full refinements at few selected temperatures and to acquire detailed measurements of the lattice parameters versus temperature. A 4-g powder sample of $Sr_{0.40}Ba_{0.60}Mn_{0.93}Ti_{0.07}O_3$ was measured at temperatures between 2.5 and 500 K using a Ge (311) monochromator with a wavelength of 2.0772 Å.

III. RESULTS AND DISCUSSION

A. Materials synthesis and phase formation

Compositions produced with various Ba and Ti amounts are summarized in Fig. 1. The c/a ratio labels indicate the samples' structural type at room temperature after their final

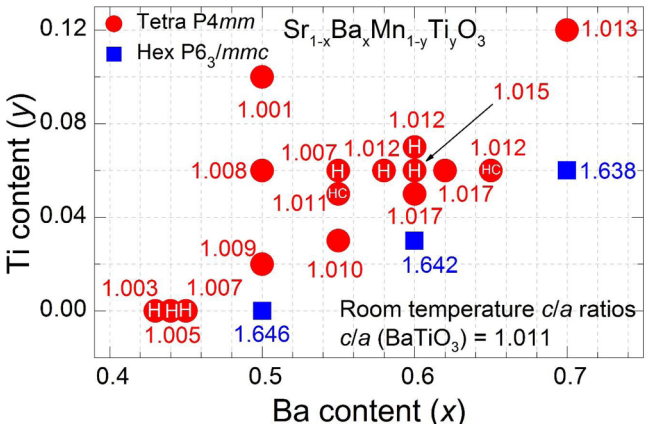

FIG. 1. Room temperature c/a ratio as a function of the Ba and Ti content. Perovskite and hexagonal phases are denoted by circles and squares, respectively. The c/a values are listed next to the symbols. The letters HC and H inside the circles indicate temperature-dependent cycles of synchrotron data collected on heating followed by cooling (HC) and heating again to above T_C (H), respectively.

annealing in pure oxygen. As shown in the figure, a well-defined region is identified in which high-purity tetragonal perovskites (full red circles) are obtained with the desired tetragonal lattice parameters c/a ratio > 1 (1.001–1.017 as shown in Fig. 1). The magnitude of this distortion is comparable to $c/a = 1.011$ of the ferroelectric $BaTiO_3$ benchmark counterpart [53], thus confirming the potential of our SBMTO materials to achieve large spontaneous polarization that can be estimated using the empirical equation $P_S^2 \propto (c/a - 1)$ [34]. It is worth emphasizing here the increased solubility of Ba from $x \sim 0.45$ for the Ti-free powder series [35] to $x \sim 0.7$ with modest Ti substitution of no more than 12% ($y = 0.12$) (this work). Samples with larger x values as a function of increasing y content could not be stabilized in the tetragonal or pseudocubic form, despite our extensive synthesis efforts under various isobaric conditions. Those compositions crystallize in the more stable hexagonal 4L structure ($c/a \gg 1$) in which (Mn, Ti)O_6 octahedra form mixed corner- and face-sharing networks [28]. Also noteworthy is the synthesis of cubic structures ($c/a \sim 1$) that remain undistorted at room temperature (not shown), within the resolution of our lab x rays, despite the significant strains and chemical pressures to which the materials are subjected to.

Representative x-ray patterns are shown in Fig. S1 (see Supplemental Material [54]) for the $x = 0.55$ and $y = 0.05$ sample before and after oxygen annealing. Large angular shifts to higher values of the diffraction peaks after oxygen annealing (i.e., smaller lattice parameters) agree with the large change in oxygen content ($\Delta\delta \sim 0.6$) and the concomitant conversion of large Mn^{3+} and Mn^{2+} ions present in the oxygen-deficient samples into smaller Mn^{4+} ions when fully oxygenated. Highly oxygen-deficient samples obtained after annealing in H_2/Ar atmospheres at 1300 °C crystallize in the common perovskite $Pm\bar{3}m$ cubic structure, indicating a random distribution of the oxygen vacancies. Here, we also note that Ba and Ti substitutions suppress the various room-temperature long-range oxygen ordered phases previously identified in oxygen-deficient $SrMnO_{3-\delta}$ materials [55]. Upon

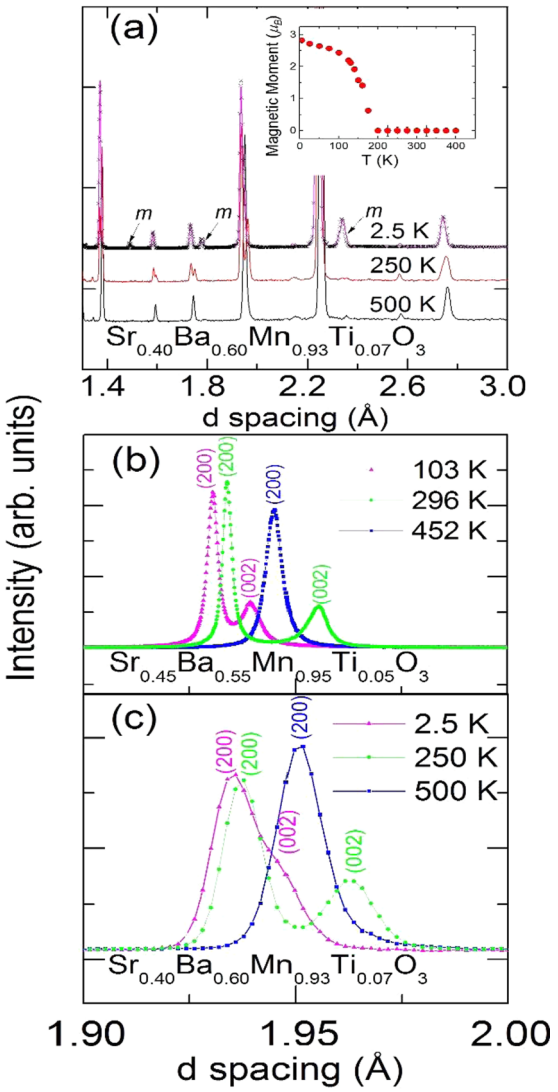

FIG. 2. (a) Neutron-diffraction patterns for $Sr_{0.40}Ba_{0.60}Mn_{0.93}Ti_{0.07}O_3$. Arrows indicate the magnetic intensities that arise from antiferromagnetic ordering below T_N. Inset shows the refined magnetic moment. Error bars indicate one standard deviation. (b) Synchrotron x-ray data (11-BM-B) showing the large splitting of cubic ⟨200⟩ Bragg peak (blue) into two tetragonal ⟨200⟩ and (002) peaks in the FE-only region at 296 K (green) and in the multiferroic region at 103 K (magenta) below $T_N \sim 155$ K. (c) Similar results observed with neutron diffraction for $Sr_{0.40}Ba_{0.60}Mn_{0.93}Ti_{0.07}O_3$ below 158 K. Please see text and Supplemental Material [54] for more details.

filling the vacancies by annealing the material in oxygen at 350 °C, the room temperature structure of our SBMTO series becomes tetragonal and crystallizes in the FE-compatible noncentrosymmetric *P*4*mm* space-group symmetry.

B. Nuclear and magnetic structural properties

Best-fit Rietveld refinements shown in Fig. 2(a) display representative patterns of the cubic and tetragonal symmetries above and below T_S observed with $Sr_{0.40}Ba_{0.60}Mn_{0.93}Ti_{0.07}O_3$ (neutrons) and $Sr_{0.45}Ba_{0.55}Mn_{0.95}Ti_{0.05}O_3$ (x rays; see Fig. S2 in the Supplemental Material [54]), respectively. At 500 K, a typical three-dimensional stacking of corner-shared (Mn, Ti)O_6 octahedra produces the paraelectric cubic phase in which (Mn,Ti) atoms occupy high-symmetry positions at the center of perfect octahedral oxygen cages. *A*-site (Sr,Ba) ions occupy the large cavities that form between the octahedra [56]. At all temperatures below T_S, strain-induced tetragonal distortions of the elongated (Mn, Ti)O_6 octahedra force the (Mn,Ti) atoms to shift along the *c* axis away from their original high-symmetry positions while both the independent apical and equatorial oxygen atoms of the octahedra shift simultaneously in the opposite direction, thus creating charge separation and ferroelectricity compatible with the noncentrosymmetric *P*4*mm* space-group symmetry of the material. Distortions observed in our SBMTO series are analogous to Ti and O displacements in $BaTiO_3$ that give rise to its robust ferroelectric displacive-type properties [57–59]. Below T_N, ordering of the Mn^{4+} magnetic sublattice gives rise to additional magnetic intensities as shown in Fig. 2(a). An AFM magnetic sublattice of the G type, insensitive to the atomic displacements of Mn or O, is best described using the $P4/m'm'm$ magnetic space-group symmetry [60] in which the magnetic moment of each Mn^{4+} ion couples antiferromagnetically with each of its six nearest neighbors. At 2.5 K, the Mn magnetic moment refined to 2.82(6) μ_B/Mn (close to the free-ion value of 3 μ_B), shown in the inset of Fig. 2(a), is in good agreement with values typically obtained for Mn^{4+} in similar manganite structures [35] and with the disruptive effects of Ti randomly occupying the same sites of the Mn sublattice. Order parameter scans of the magnetic peak (½ ½ ½) are shown in Fig. S3 (see Supplemental Material [54]).

Splitting of the cubic $\langle 200\rangle_C$ peak into two tetragonal $(002)_T$ and $\langle 200\rangle_T$ reflections at 296 K (x rays) and 250 K (neutrons) is shown in Figs. 2(b) and 2(c). The figure also demonstrates reduced peak splitting below T_N, indicating partial suppression of the ferroelectric tetragonal order as it competes with magnetism and the coexistence of the two order parameters down to 2.5 K. This observation contrasts with the near complete suppression of the tetragonal order in the Ti-free $Sr_{1-x}Ba_xMnO_3$ counterparts [34,35] and demonstrates the sensitivity of the FE order to tiny variations of the Ba and/or Ti content. More evidence of magnetoelectric tunability is shown in additional measurements presented below. Structural parameters and relevant bond lengths and angles obtained from refinements using oxygen-sensitive neutron data are listed in Table S1 (see Supplemental Material [54]). The in-plane Mn-O2-Mn bond angle of 177.4° at 2.5 K agrees with AFM exchange interactions [31,40].

C. First-order ferroelectric order parameter

Synchrotron x-ray data collected on heating between 80 and 452 K were used to determine the exact temperatures at which structural and magnetic transitions occur. Shown in Fig. 3(a) are diffraction color maps for three compositions in which the Ti content was kept constant ($y = 0.06$) while the Ba concentration varied slightly, namely, $x = 0.55$, 0.58, 0.60. Monitoring the behavior of the tetragonal (002) and ⟨200⟩ diffraction peaks demonstrates the steep character of the cubic-to-tetragonal phase transition line with T_S rising by

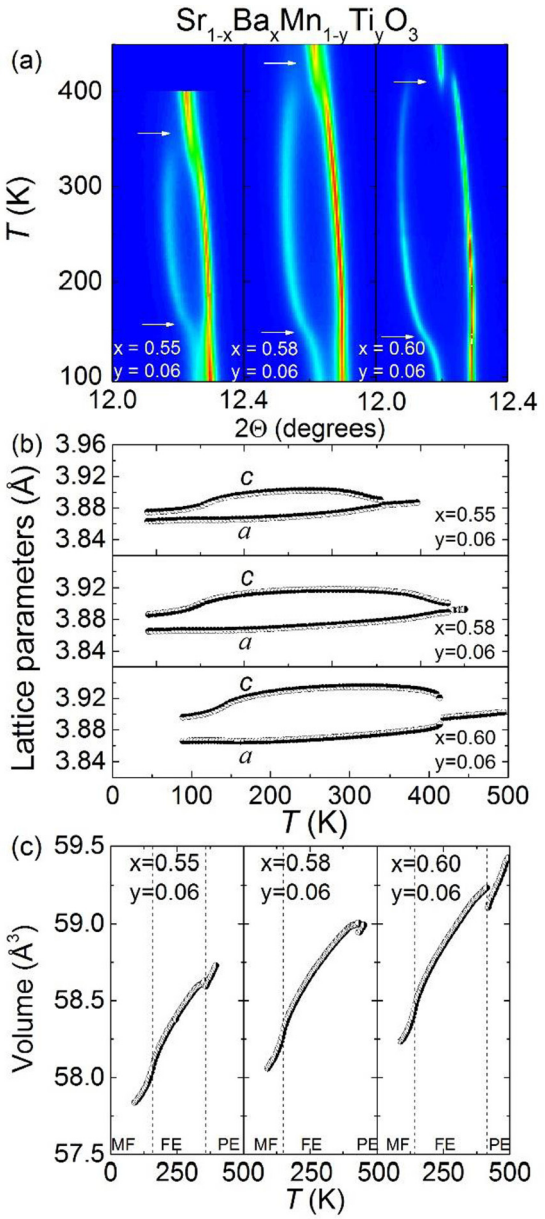

FIG. 3. (a) Color maps of synchrotron x-ray data (11-BM-B) near the tetragonal (002) and ⟨200⟩ diffraction peak taken upon heating for $Sr_{1-x}Ba_xMn_{1-y}Ti_yO_3$ samples with fixed Ti content $y = 0.06$ and Ba contents changing slightly from $x = 0.55$ (a), to 0.58 (b) and 0.60 (c). Top and bottom arrows indicate T_C and T_N, respectively. (b) Temperature evolution upon heating of the lattice parameters for $Sr_{1-x}Ba_xMn_{1-y}Ti_yO_3$ samples with $x = 0.60$, 0.58, 0.55 and $y = 0.06$. (c) Temperature dependence of the reduced unit-cell volume for $x = 0.55-0.60$ and $y = 0.06$ demonstrating the first-oder nature of the ferroelectric phase transition.

about 80 K, from 350 to 430 K, as a function of increasing Ba. The latter is higher than T_S values obtained with Ti-free $Sr_{1-x}Ba_xMnO_3$ [35] or bulk $BaTiO_3$ [57–59]. Concurrently, the FE tetragonal distortions increase rapidly with increasing Ba, as seen in the progressively larger peak separation in Fig. 3(a) and in the corresponding refined lattice parameters shown in Fig. 3(b). The unit-cell volume undergoes an abrupt discontinuity at the structural transition temperature

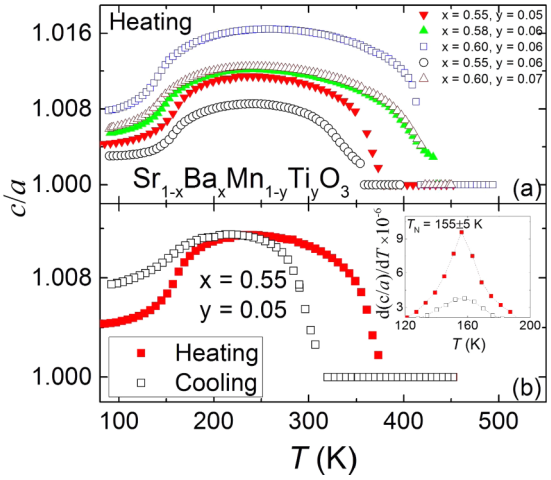

FIG. 4. (a) Strain (c/a) vs temperature for compositions $x = 0.55-0.60$ and $y = 0.05-0.07$ during heating cycle. (b) Strain (c/a) vs temperature for the $Sr_{0.45}Ba_{0.55}Mn_{0.95}Ti_{0.05}O_3$ sample during a heating and cooling cycle. Hystertic behaviors are observed, but the maximum c/a ratio remains unaffected (see temperature derivative of the c/a ratio in the inset).

T_S—see, for example, Fig. 3(c) for the $x = 0.60$ and $y = 0.06$ sample—in agreement with first-order transition between the paraelectric and ferroelectric phases.

On the other hand, increasing the Ti content ($y = 0.06$, 0.07) while keeping the Ba content fixed (at $x = 0.60$, for example) appears to result in smaller tetragonal structural distortions, as shown in Fig. 4(a) (c/a ratio) and Fig. S4(a) (color maps) (see Supplemental Material [54]), for example. The results agree with Fig. 1, which shows the tetragonality decreasing as a function of increasing Ti content (y). Excellent agreement is observed between the lattice parameters obtained using neutrons (red squares) and x rays (blue triangles) for the $x = 0.60$, $y = 0.07$ sample, Fig. S4(b) (see Supplemental Material [54]).

The first-order character of the phase transitions was further examined by measuring the hysteresis properties of another sample with a slightly different composition, namely, the $x = 0.55$ and $y = 0.05$ sample, Fig. 5. First, the sample was fast cooled to ∼80 K and measurements collected on heating to 452 K, then on cooling back to 80 K. A first-order-like hysteresis of the FE order is observed, with the transition temperature T_S shifting from ∼374 K on heating to ∼314 K on slow cooling. While the 60-K hysteresis is an order of magnitude larger than that of $BaTiO_3$ (∼6 K hysteresis) [61], we note that the material remains ferroelectric at room temperature. More importantly, the wide hysteresis does not affect the maximum tetragonal distortion as it remains largely unchanged with $c/a \sim 1.0115$ near 225 K, as revealed by the temperature-dependent lattice parameters and c/a ratio displayed in Figs. 5(b) and 4(b), respectively. Below T_N, the c/a ratio and the out-of-plane lattice parameter (c) are partially suppressed while the in-plane lattice parameter (a) increases slightly and the structure remains tetragonal down to the lowest measured temperature (10 K as in Ti-free $Sr_{1-x}Ba_xMnO_3$ [35] and 2.5 K for the $x = 0.6$, $y = 0.07$ sample discussed above). Intriguingly, the c/a ratio was noticeably less

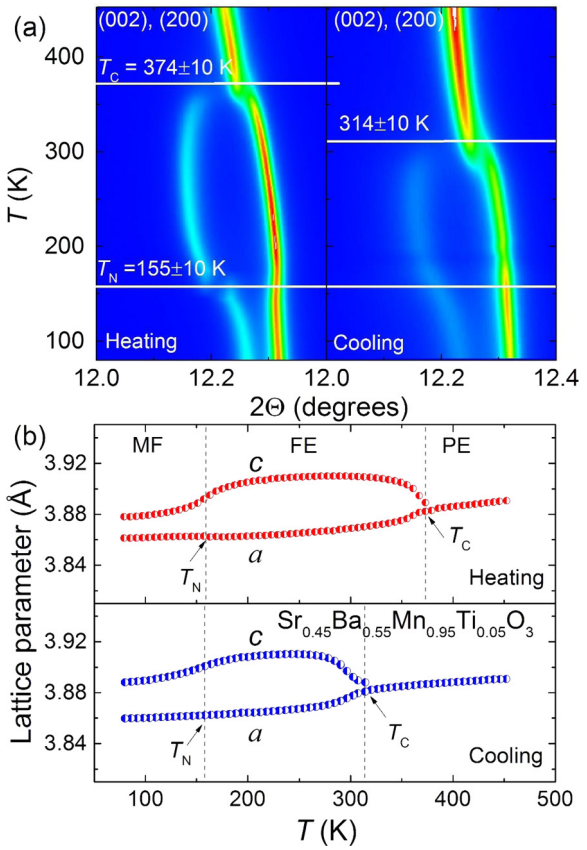

FIG. 5. Two-dimensional color maps of raw synchrotron x-ray data (11-BM-B) (a) and the refined lattice parameters (b) for $Sr_{0.45}Ba_{0.55}Mn_{0.95}Ti_{0.05}O_3$. The top panel shows the FE-induced splitting of the cubic ⟨200⟩ reflection and its attempt for recovery below T_N when the ferroelectric order is partially suppressed.

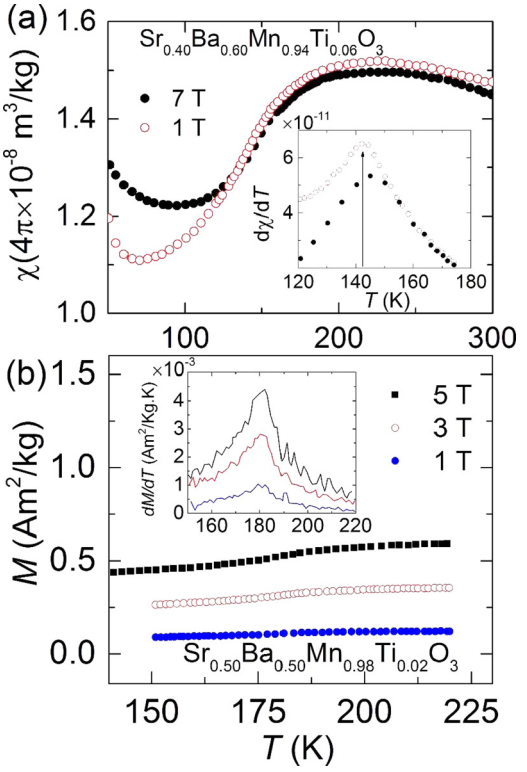

FIG. 6. (a) Magnetic susceptibility of $Sr_{0.40}Ba_{0.60}Mn_{0.94}Ti_{0.06}O_3$ vs temperature in external magnetic fields of 1.0 and 7.0 T. Néel temperature of 142 ± 5 K is shown in the inset. (b) Temperature derivatives of dc magnetization data (see inset) collected at ambient pressure for $Sr_{0.50}Ba_{0.50}Mn_{0.98}Ti_{0.02}O_3$ in applied magnetic fields of 1.0, 3.0, and 5.0 T.

suppressed on cooling (1.007 at 80 K, 40%) than on heating (1.004, 65%). While various arguments could be invoked to explain this behavior (e.g., saturated polarization achieved on slow cooling versus unsaturated room temperature polarization of the relatively fast cooled as-made samples), it is clear that *in situ* work under various temperature and atmospheric conditions would be needed to study the thermal and temporal effects on the magnitude and stability of the FE order.

On the other hand, temperatures of full phase transition to bulk magnetism obtained from the temperature derivatives of the c/a curves agree well with the magnetic measurements discussed below. The nonhysteretic Néel transition temperature $T_N \sim 155$ K [see inset of Fig. 4(b)] observed on cooling and on heating confirms the second-order nature of the magnetic transition.

D. Magnetic properties

Figure 6 shows the temperature dependence of ac susceptibility for the $x = 0.60$ and $y = 0.06$ sample measured in external magnetic fields of 1.0 and 7.0 T. The temperature derivative of magnetic susceptibility, $(d\chi/dT)$, was used to define the essentially field-independent magnetic transition temperature T_N at 142 ± 5 K [see inset of Fig. 6(a)]. Figure 6(b) displays dc magnetization curves for a second sample with $x = 0.50$ and $y = 0.02$ at 1.0, 3.0, and 5.0 T. The dc magnetization, growing significantly with increased fields, exhibits better-defined AFM transitions. Temperature derivatives of the magnetization (dM/dT), shown in the inset of Fig. 6(b), were used to determine an essentially unchanged $T_N \sim 180$ K, which again did not exhibit much dependence on the magnitude of the applied magnetic field. T_N values obtained by magnetic measurements are in agreement with those structurally determined from c/a temperature derivatives, Table S2 (see Supplementary Material [54]).

A linear suppression of T_N from ∼188 to ∼133 K is shown in Fig. 7(b) as a function of increasing Ba content ($x = 0.45-0.65$) at a fixed Ti concentration $y = 0.06$. This behavior agrees well with the Ti-free $Sr_{1-x}Ba_xMnO_3$ series for which a similar linearity was successfully correlated with *A*-site ionic-size-variance–induced structural disorder and the local variations of the strained Mn-O_2-Mn bond angles [31,34]. We note, however, that while the Ba content effects on T_N are clear, we observe no obvious trends between Ti ($y = 0$, 0.02, 0.06, and 0.10) and T_N (see Fig. S5 in the Supplemental Material [54]) at fixed Ba content (e.g.,$x = 0.50$), Table S2 (see Supplemental Material [54]).

E. Spontaneous polarization and tunable magnetoelectric coupling

Figure 4(a) shows reduction of the $(c/a - 1)$ ratio below T_N by about 55%−65% for a few select compositions (e.g.,

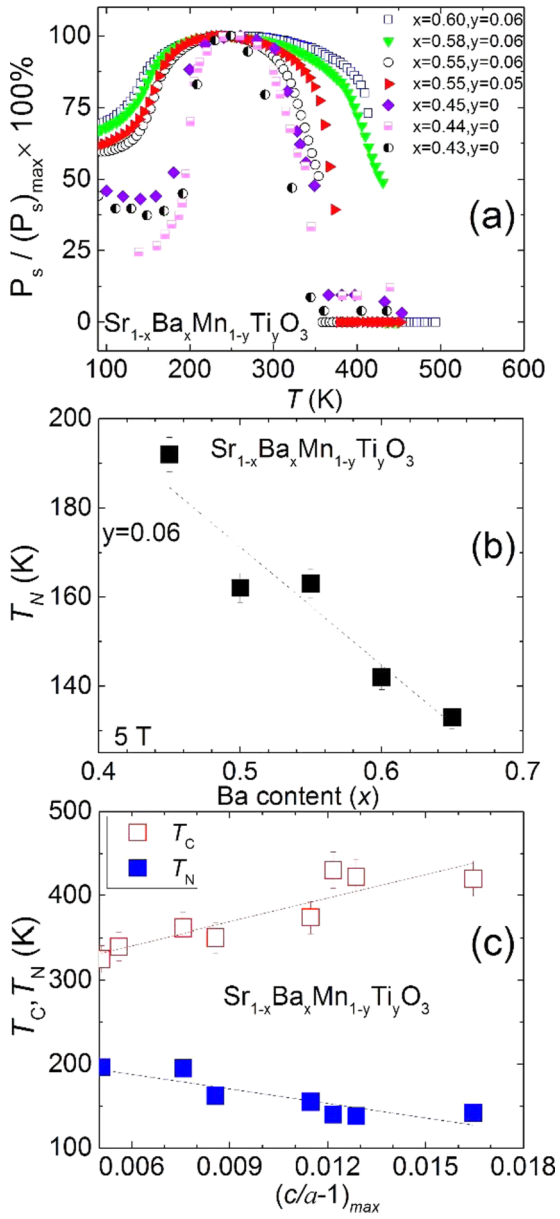

FIG. 7. (a) Ratio of the spontaneous polarization calculated using the empirical relation $P_S^2 \propto (c/a-1)$ vs temperature for compositions $x = 0.43-0.60$ and $y = 0-0.06$. (b) T_N vs Ba content (x) with fixed Ti content $y = 0.06$ (from magnetization measurements at 5.0 T) showing the linear suppression of T_N as a function of x (Ba content). (c) (T_C, T_N) vs the maximum tetragonal distortion $(c/a-1)_{max}$ [extracted from the top panel 7(a)] for compositions $x = 0.43-0.60$ and $y = 0-0.06$ during the heating cycle. Error bars represent one standard deviation.

$0.008/0.016 = 50\%$ for the $x = 0.6$, $y = 0.06$ sample (blue squares), for example). All samples measured by diffraction exhibited similar kinks in their c/a curves, indicating the partial suppression of ferroelectricity. The large tetragonal order surviving to the lowest measured temperature is in stark contrast with data previously reported for $Sr_{1-x}Ba_xMnO_3$ (Fig. 13 of Ref. [35]) in which the suppression of tetragonality at first appears complete. If accurate, however, the ferroelectric order would have been fully destroyed, with P_S dropping to zero, giving way to the low-temperature AFM cubic state in $Sr_{1-x}Ba_xMnO_3$. However, Rietveld refinements confirmed the persistence of a slightly distorted tetragonal FE phase below T_N with $(c/a-1)$ reduced by about 90% of its maximum strength [35]. Consequently, a 56% P_S suppression would be expected, despite the small c/a ratio, by using the empirical relation $P_S^2 \propto (c/a-1)$. Indeed, calculations of P_S using the refined bond lengths and angles in a point charge model [35] resulted in substantial P_S of $\sim 13.4\,\mu C/cm^2$ at ~ 195 K for the $x = 0.45$ sample ($y = 0$), in agreement with Sakai's measured P_S value of $13.5\,\mu C/cm^2$ at 2.5 K [34] for a similar sample. This corresponds to about 55% suppression of the maximum $P_S = 29.54\,\mu C/cm^2$ observed at ~ 225 K.

In the case of $Sr_{0.4}Ba_{0.6}Mn_{0.93}Ti_{0.07}O_3$, the c/a ratios of 1.0057 and 1.0128 at 2.5 and 250 K, respectively, indicate significantly less suppression of the tetragonal distortion ($\sim$55%) than in the Ti-free counterparts ($\sim$90%). The equation $P_S^2 \propto (c/a-1)$ suggests a P_S reduction of $\sim$34% between the same two temperatures, in relative agreement with the 47% P_S suppression calculated using the refined bond lengths and angles (P_S reduced from $\sim 28.95\,\mu C/cm^2$ at 250 K to $15.19\,\mu C/cm^2$ at 2.5 K). This is a remarkable agreement considering the standard errors associated with least-squares refinements that affect the absolute accuracy of both the lattice parameters and the internal structural parameters. However, direct measurements of P_S from FE hysteresis loops were unsuccessful due to leakage currents as well as the polycrystalline nature of the samples, similar to $Sr_{1-x}Ba_xMnO_3$ samples.

Finally, examining the relative spontaneous polarization (P_S/P_S^{max}) for all the samples including our previously reported Ti-free samples [35] establishes the explicit effects of

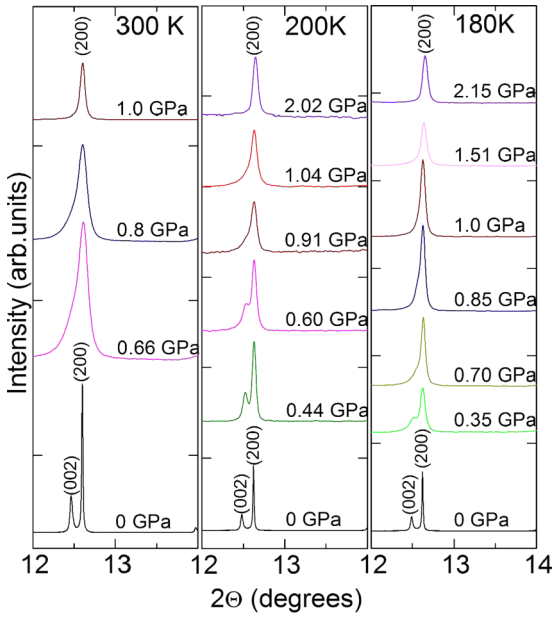

FIG. 8. Tetragonal to cubic structural transition as a function of applied pressure at various temperatures. Data at ambient pressure was collected on beamline 11-BM-B. At high pressures, data collected at 16-BM-D. See text for details.

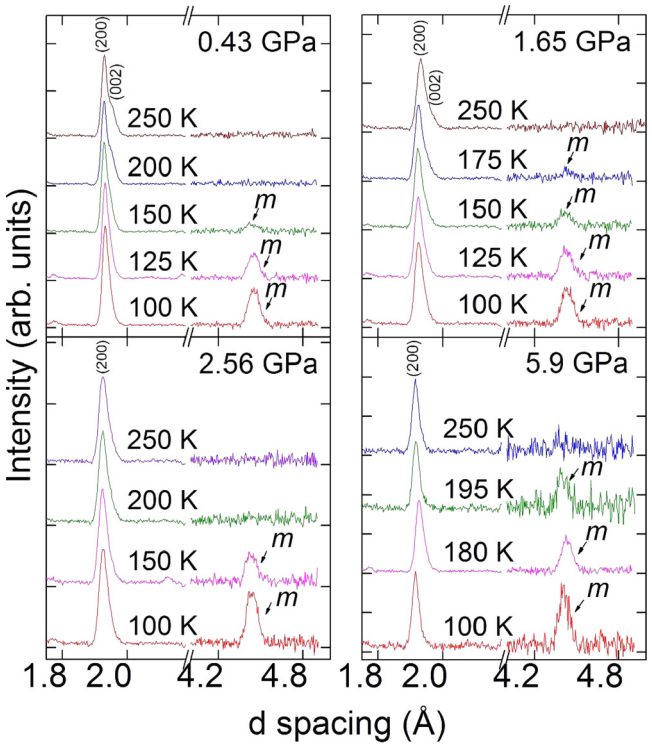

FIG. 9. Representative NPD data (SNAP) for $Sr_{0.45}Ba_{0.55}Mn_{0.95}Ti_{0.05}O_3$ showing the structural transition from tetragonal to cubic in the form of suppressed peak splitting and enhanced T_N (1.75–2.0 Å). The pressure-induced cubic phase is magnetic, as shown in the magnetic reflection observed between 4.2 and 4.8 Å. The letter "m" indicates the observed temperature-dependent magnetic peak.

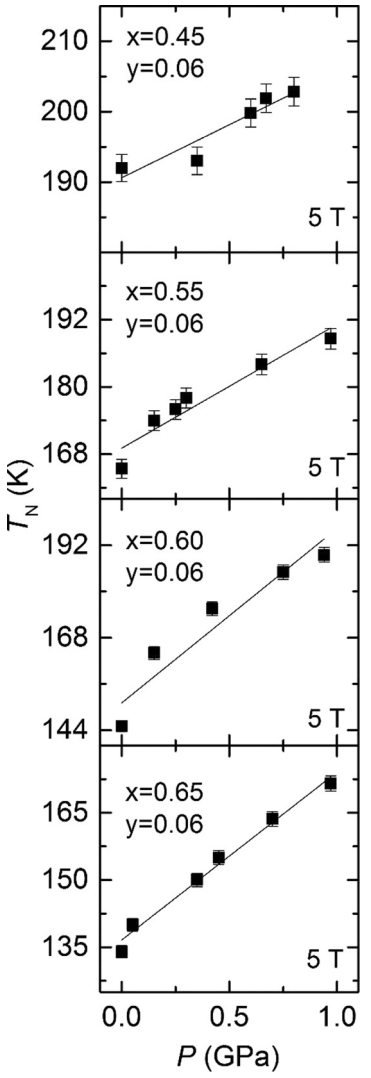

FIG. 10. P-T_N plots showing the increase of Néel temperature with applied pressure at 5.0 T for $Sr_{1-x}Ba_xMn_{1-y}Ti_yO_3$ ($x = 0.45$, 0.55, 0.60, 0.65 and $y = 0.06$). Error bars represent one standard deviation.

Ba and Ti substitution on both the FE and AFM properties of the system with the former order parameter peaking at about 225 K, Fig. 7(a). The figure further demonstrates the widening of the operational temperature range that separates the two order parameters and more importantly, the tunable character of the magnetoelectric coupling in response to tiny variations of the *A*-site or *B*-site stoichiometry. Figures 4(a) and 7(a) and various magnetization measurements (data not shown) reveal linear trends between T_N and the Ba content at fixed Ti substitution levels [see Fig. 7(b)] and between T_C or T_N versus the maximum tetragonal distortion $(c/a - 1)_{max}$, Fig. 7(c).

F. Structural and magnetic properties under pressure

A good understanding of the multiferroic order parameter coupling could be achieved by determining the response to pressure of the FE-induced tetragonal distortions and whether or not their possible suppression would lead to enhanced magnetic properties. $Sr_{0.45}Ba_{0.55}Mn_{0.95}Ti_{0.05}O_3$ was selected for diffraction studies under hydrostatic pressures up to 5.9 GPa, Figs. 8 and 9. For reference, the Curie temperature of nonmagnetic $BaTiO_3$ is known to decrease linearly with increasing pressure at the rate of 70 K/GPa [62]. The magnetic properties of four additional samples, examined up to 1.0 GPa pressure, demonstrate the universal character of this multiferroic series, Fig. 10, with the T_N increasing linearly at the rate of 10–20 K/GPa as a function of increased pressure.

Measurements performed at 16-BM-D demonstrate the suppression of the FE order parameter under pressure as seen in the recombination of tetragonal ⟨200⟩ and (002) reflections into single cubic ⟨200⟩ peaks. A representative synchrotron x-ray pattern under pressure is shown in Fig. S6 (see Supplemental Material [54]) in the 2θ angular range of $8^\circ - 14^\circ$. Patterns displayed in Fig. 8 demonstrate the gradual suppression of the tetragonal order parameter upon increased pressure. Reference ambient-pressure x-ray patterns in the figure were recorded at the high-resolution 11-BM-B diffractometer. Peak recombination and the full suppression of the FE order is achieved at the measured pressures of ∼1.5, 2.0, and 1.0 GPa at 180, 200, and 300 K, respectively.

X rays alone cannot directly reveal the magnetic properties of the high-pressure cubic phase and if the

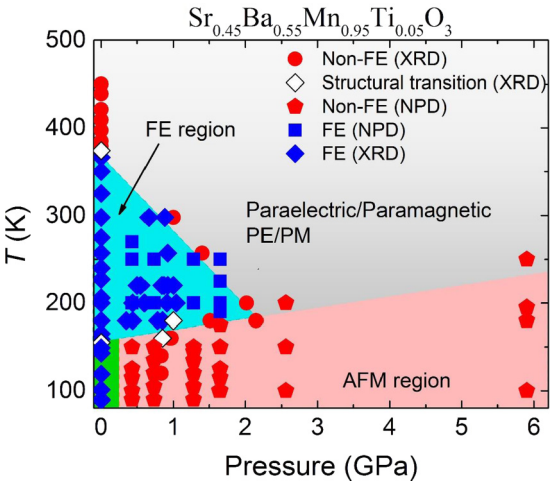

FIG. 11. Pressure-temperature (P-T) phase diagram for $Sr_{0.45}Ba_{0.55}Mn_{0.95}Ti_{0.05}O_3$. Dark cyan represents the ferroelectric-only tetragonal region; no magnetic order observed in this region. Light magenta represents pressure-induced cubic and magnetic region. Green shaded polygon delineates the multiferroic region estimated from neutron and x-ray measurements.

low-temperature magnetic order would survive the applied pressure. Hence, a neutron powder diffraction experiment was performed on SNAP using the same $x = 0.55$ and $y = 0.05$ sample at various pressures and temperatures between 90 and 250 K. Figure 9 exhibits the relevant neutron powder diffraction (NPD) pattern portions in the d-spacing range of 1.75–4.8 Å. Within the resolution of SNAP, the tetragonal ⟨200⟩ and (002) peaks are observed at temperatures between 150 and 250 K at the moderate pressures of 0.43 and 0.73 GPa. No sign of any tetragonal splitting is observed at any temperature for pressures exceeding 2.56 GPa.

Combining the pressure- and temperature-dependent neutron and x-ray results enabled the construction of a detailed pressure-temperature (P-T) phase diagram, displayed in Fig. 11. The phase diagram exposes the fragile character of the ferroelectric tetragonal order, which is relatively easily suppressed in the nonmagnetic state at temperatures near 300 K. Our data reveal the same T_C suppression rate of ∼70 K/GPa as the analogous $BaTiO_3$ [62], which is rather remarkable considering that the electronic properties of the Ti^{4+} d^0 ions and Mn^{4+} d^3 ions are quite different. On the other hand, the low-temperature tetragonal symmetry, below T_N, is suppressed under low pressures of no more than 0.4–0.8 GPa. As shown in Fig. 11, an ambient-pressure T_N of $\sim 155 \pm 5$ K determined from the temperature derivative of the c/a ratio is enhanced at the rate of ∼10−20 K/GPa upon increasing the applied pressure, in agreement with the pressure-dependent AFM properties shown in Fig. 10. Noticeably, the linear T_N enhancement should reach ∼240 K at 5.9 GPa, as measured by NPD data shown in Fig. 9 and expected from the high-pressure magnetic measurements described earlier. The P-T phase diagram demonstrates that suppression of the ferroelectric tetragonal order in the multiferroic region is even stronger than in the nonmagnetic state due to enhancement of AFM properties under pressure.

IV. CONCLUSIONS

Extensive investigations of optimal synthesis conditions enabled the creation of a new series of multiferroic perovskites in which the Ba solubility at the Sr site of $SrMnO_3$ is extended to previously forbidden limits. The extended solubility was facilitated by the simultaneous introduction of dilute amounts of nonmagnetic Ti at the Mn site and the development of elaborate multistep synthesis procedures. Most of the compositions prepared for this work exhibit the desired multiferroic properties, characterized by the stabilization of noncentrosymmetric tetragonal symmetry below T_C's as high as ∼430 K and the coexistence of the FE order with magnetism at lower temperatures. Using a series of scattering experiments, we successfully demonstrate the tunable character of coupling between the magnetic and FE order parameters. This is evidenced by the tunability of the FE suppression by applying external pressures or by varying the internal chemical pressure using different substitution amounts of Ba and Ti. With Ti substitution, we were able to decrease T_N and suppress AFM interactions in favor of the FE order extending into the multiferroic state. The Ti substitution did not, however, sufficiently eliminate leakage currents to permit direct measurements of the spontaneous polarization by electrical measurements of P-E curves.

Our measurements of the magnetic and structural properties under pressure allowed the construction of a detailed P-T phase diagram in which the diverse phases are clearly delineated. Most importantly, our results show that relatively low to moderate pressures suffice to enhance the magnetic order at the expense of ferroelectricity and that the process is reversible. The ferroelectric transition is of the first order, as characterized by the significant hysteresis observed in high-resolution synchrotron data with the order parameter universally peaking at a temperature close to 225 K, regardless of composition. Impressive spontaneous polarization values of $\sim 30\,\mu C/cm^2$, in agreement with Ti-free $Sr_{1-x}Ba_xMnO_3$, are calculated using either the c/a-based empirical equation or the Mn-O bond lengths and bond angles obtained from neutron diffraction and Rietveld refinements.

ACKNOWLEDGMENTS

The authors wish to thank Sergey Tkachev for his assistance with loading the DAC cells for the APS measurements. Work conducted at the Materials Science Division at Argonne National Laboratory (O.C. and S.R., neutron scattering and structural analysis) was supported by the U.S. DOE, Office of Science, Materials Sciences and Engineering Division. Part of this research conducted at ORNL's Spallation Neutron Source was sponsored by the Scientific User Facilities Division, Office of Basic Energy Sciences, U.S. Department of Energy. Use of the Advanced Photon Source at Argonne National Laboratory was supported by the U.S. Department of Energy, Office of Science, Office of Basic Energy Sciences, under Contract No. DE-AC02-06CH11357. HPCAT operations are supported by DOE-NNSA's Office of Experimental Sciences. B.D. (materials synthesis), J.P., E.M., and B.A. (magnetic and electrical measurements) were supported by the Polish NCN through Grant No. 2018/31/B/ST5/03024.

[1] C. Zener, Phys. Rev. **82**, 403 (1951).
[2] R. E. Cohen, Nature (London) **358**, 136 (1992).
[3] J. Junquera and P. Ghosez, Nature (London) **422**, 506 (2003).
[4] H. Schmid, Ferroelectrics **162**, 317 (1994).
[5] T. Kimura, T. Goto, H. Shintani, and K. Ishizaka, Nature (London), **426**, 55 (2003).
[6] R. Ramesh and N. A. Spaldin, Nat. Mater. **6**, 21 (2007).
[7] J. Wang, J. B. Neaton, H. Zheng, V. Nagarajan, S. B. Ogale, B. Liu, D. Viehland, V. Vaithyanathan, D. G. Schlom, U. V. Waghmare, N. A. Spaldin, K. M. Rabe, M. Wuttig, and R. Ramesh, Science **299**, 1719 (2003).
[8] K. F. Wang, J. M. Liu, and Z. F. Ren, Advs. Phys. **58**, 321 (2009).
[9] N. A. Hill, J. Phys. Chem. B **104**, 6694 (2000).
[10] T. Kimura, S. Kawamoto, I. Yamada, M. Azuma, M. Takano, and Y. Tokura, Phys. Rev. B **67**, 180401 (2003).
[11] C. J. Fennie and K. M. Rabe, Phys. Rev. B **72**, 100103 (2005).
[12] M. Feibig, T. Lottermoser, D. Frohlich, A. V. Goltsev, and R. V. Pisarev, Nature (London) **419**, 818 (2002).
[13] B. B. Van Aken, T. T. M. Palstra, A. Filippetti, and N. A. Spaldin, Nat. Mater. **3**, 164 (2004).
[14] Y. Yamasaki, H. Sagayama, T. Goto, M. Matsuura, K. Hirota, T. Arima, and Y. Tokura, Phys. Rev. Lett. **98**, 147204 (2007).
[15] S.-W. Cheong and M. Mostovov, Nat. Mater. **6**, 13 (2007).
[16] D. Khomskii, Physics **2**, 20 (2009).
[17] W. D. Ratcliff, J. W. Lynn, V. Kiryukhin, P. Jain, and M. R. Fitzsimmons, npj Quantum Mater. **1**, 16003 (2016).
[18] C. Ederer and N. A. Spaldin, Phys. Rev. B **71**, 060401(R) (2005).
[19] M. Bibes and A. Barthelemy, Nat. Mater. **7**, 425 (2008).
[20] J. S. Hwang, J. Y. Cho, S. Y. Park, Y. J. Yoo, P. S. Yoo, B. W. Lee, and Y. P. Lee, Appl. Phys. Lett. **106**, 062902 (2015).
[21] M. D. Casper, M. D. Losego, and J. P. Maria, J. Mater. Sci. **48**, 1578 (2012).
[22] N. Waterfield Price, A. M. Vibhakar, R. D. Johnson, J. Schad, W. Saenrang, A. Bombardi, F. P. Chmiel, C. B. Eom, and P. G. Radaelli, Phys. Rev. Appl. **11**, 024035 (2019).
[23] S. Bhattacharjee, E. Bousquet, and P. Ghosez, Phys. Rev. Lett. **102**, 117602 (2009).
[24] J. H. Lee and K. M. Rabe, Phys. Rev. Lett. **104**, 207204 (2010).
[25] J. M. Rondinelli, A. S. Eidelson, and N. A. Spaldin, Phys. Rev. B **79**, 205119 (2009).
[26] G. Giovannetti, S. Kumar, C. Ortix, M. Capone, and J. Van Den Brink, Phys. Rev. Lett. **109**, 107601 (2012).
[27] R. Nourafkan, G. Kotliar, and A. M. S. Tremblay, Phys. Rev. B **90**, 220405 (2014).
[28] T. Negas and R. Roth, J. Solid State Chem. **3**, 323 (1971).
[29] U. Aschauer, R. Pfenninger, S. M. Selbach, T. Grande, and N. A. Spaldin, Phys. Rev. B **88**, 054111 (2013).
[30] H. Y. Hwang, S.-W. Cheong, P. G. Radaelli, M. Marezio, and B. Batlogg, Phys. Rev. Lett. **75**, 914 (1995).
[31] O. Chmaissem, B. Dabrowski, S. Kolesnik, J. Mais, D. E. Brown, R. Kruck, P. Prior, B. Pyles, and J. D. Jorgensen, Phys. Rev. B **64**, 134412 (2001).
[32] L. M. Rodriguez-Martinez and J. P. Attfield, Phys. Rev. B **54**, R15622(R) (1996).
[33] R. D. Shannon, Acta Crystallogr., Sect. A: Found. Crystallogr. **32**, 751 (1976).
[34] H. Sakai, J. Fujioka, T. Fukuda, D. Okuyama, D. Hashizume, F. Kagawa, H. Nakao, Y. Murakami, T. Arima, A. Q. R. Baron, Y. Taguchi, and Y. Tokura, Phys. Rev. Lett. **107**, 137601 (2011).
[35] H. Somaily, S. Kolesnik, J. Mais, D. Brown, K. Chapagain, B. Dabrowski, and O. Chmaissem, Phys. Rev. Mater. **2**, 054408 (2018), and the references within.
[36] D. K. Pratt, J. W. Lynn, J. Mais, O. Chmaissem, D. E. Brown, S. Kolesnik, and B. Dabrowski, Phys. Rev. B **90**, 140401 (2014).
[37] V. Goian, E. Langenberg, N. Marcano, V. Bovtun, L. Maurel, M. Kempa, T. Prokscha, J. Kroupa, P. A. Algarabel, J. A. Pardo, and S. Kamba, Phys. Rev. B **95**, 075126 (2017).
[38] V. Goian, F. Kadlec, C. Kadlec, B. Dabrowski, S. Kolesnik, O. Chmaissem, D. Nuzhnyy, M. Kempa, V. Bovtun, M. Savinov, J. Hejtmanek, J. Prokleska, and S. Kamba, J. Phys.: Condens. Matter **28**, 175901 (2016).
[39] H. Sakai, J. Fujioka, T. Fukuda, M. S. Bahramy, D. Okuyama, R. Arita, T. Arima, A. Q. R. Baron, Y. Taguchi, and Y. Tokura, Phys. Rev. B **86**, 104407 (2012).
[40] B. Dabrowski, S. Kolesnik, O. Chmaissem, L. Suescun, and J. Mais, Acta Phys. Pol., A **111**, 15 (2007).
[41] B. Dabrowski, O. Chmaissem, J. Mais, S. Kolesnik, J. D. Jorgensen, and S. Short, J. Solid State Chem. **170**, 154 (2003).
[42] C. Park, D. Popov, D. Ikuta, C. Lin, C. Kenney-Benson, E. Rod, Arunkumar Bommannavar, and G. Shen, Rev. Sci. Instrum. **86**, 072205 (2015).
[43] C. Prescher and V. B. Prakapenka, High Pressure Res. **35**, 223 (2015).
[44] M. Rivers, V. B. Prakapenka, A. Kubo, C. Pullins, C. M. Holl, and S. D. Jacobsen, High Pressure Res. **28**, 273 (2008).
[45] A. Dewaele, M. Torrent, P. Loubeyre, and M. Mezouar, Phys. Rev. B **78**, 104102 (2008).
[46] H. K. Mao, J. Xu, and P. M. Bell, J. Geophys. Res. **91**, 4673 (1986).
[47] S. V. Sinogeikin, J. S. Smith, E. Rod, C. Lin, C. Kenney-Benson, and G. Shen, Rev. Sci. Instrum. **86**, 072209 (2015).
[48] S. Calder, K. An, R. Boehler, C. R. Dela Cruz, M. D. Frontzek, M. Guthrie, B. Haberl, A. Huq, S. A. J. Kimber, J. Liu, J. J. Molaison, J. Neuefeind, K. Page, A. M. dos Santos, K. M. Taddei, C. Tulk, and M. G. Tucker, Rev. Sci. Instrum. **89**, 092701 (2018).
[49] O. Arnold, J. C. Bilheux, J. M. Borreguero, A. Buts, S. I. Campbell, L. Chapon, M. Doucet, N. Draper, R. Ferraz Leal, M. A. Gigg, V. E. Lynch, A. Markvardsen, D. J. Mikkelson, R. L. Mikkelson, R. Miller, K. Palmen, P. Parker, G. Passo, T. G. Perring, P. F. Peterson, S. Ren, M. A. Reuter, A. T. Savici, J. W. Taylor, R. J. Taylor, R. Tolchenov, W. Zhou, and J. Zikovsky, Nucl. Instrum. Methods Phys. Res. Sec. A **764**, 156, (2014).
[50] A. C. Larson and R. B. Von Dreele, General Structure Analysis System (GSAS), Los Alamos National Laboratory Report LAUR 86-748 (2000).
[51] B. H. Toby, J. Appl. Crystallogr. **34**, 210 (2001).
[52] J. W. Lynn, Y. Chen, S. Chang, Y. Zhao, S. Chi, W. Ratcliff, B. G. Ueland, and R. W. Erwin, J. Res. NIST **117**, 61 (2012).
[53] J. H. Kwei, A. C. Lawson, and S. J. L. Billinge, J. Phys. Chem. **97**, 2368 (1993).
[54] See Supplemental Material at http://link.aps.org/supplemental/10.1103/PhysRevMaterials.3.084401 for additional x-ray and neutron powder diffraction data, Rietveld refinement with structural parameters, and bond lengths.

[55] L. Suescun, O. Chmaissem, J. Mais, B. Dabrowski, and J. D. Jorgensen, J. Solid State Chem. **180**, 1698 (2007).
[56] J. S. Zhou and J. B. Goodenough, Phys. Rev. Lett. **94**, 065501 (2005).
[57] B. Matthias and A. Von Hippel, Phys. Rev. **73**, 1378 (1948).
[58] Landolt-Börnstein, *Numerical Data and Functional Relationships in Science and Technology* (Springer, Berlin, 1981), Vol. III/16a, p. 421.
[59] Y. L. Li, L. E. Cross, and L. Q. Chen, J. Appl. Phys. **98**, 064101 (2005).
[60] H. Wondratschek and U. Müller (eds.), *International Tables for Crystallography*, Vol. A1: Symmetry Relations between Space Groups, 2nd ed. (John Wiley & Sons, Ltd., Chichester, 2010).
[61] F. Jona and G. Shirane, *Ferroelectric Crystals* (Dover Publications, Inc., New York, 1993), p. 126.
[62] G. A. Samara, Phys. Rev. **151**, 378 (1966).